Microscopic analysis of oxide formed on ZIRLO® cladding tube

Ho Yeon Bae, Chi Bum Bahn*
School of Mechanical Engineering, Pusan National University,
Busandaehak-ro 63beon-gil, Geumjeong-gu Busan. 609-735 - Republic of Korea
**Corresponding author: bahn@pusan.ac.kr*

1. Introduction

Corrosion of zirconium fuel cladding in high temperature water has limited recent efforts to prolong lifetime and reloading cycles of the fuel for enhanced plant economics. To understand corrosion mechanism of Zr alloy, a considerable literature has been devoted to microstructural studies. In ZIRLO® samples close to kinetic transition, a large variation in the sub-oxide width at different metal/oxide interface locations are observed, and this fact suggests that the transition is an extremely local process [1]. The oxide transition has been proposed to be caused by accumulated stresses during oxide growth and interconnected porosity [2]. The metal/oxide interface roughness is linked to location of cracks [3], formation of the cracks is also associated with the transition of the oxide [3,4] and large compressive stresses caused by oxide volume expansion [5,6,7]. The cracks found in the oxide are mainly oriented parallel to the metal/oxide interface. They are more likely to work as obstacles for diffusion of oxidizing species rather than as easy diffusion paths [8]. Bossis et al. reported a porous outer layer in a pre-transition oxide by ion mass spectrometry (SIMS) and electrical impedance spectroscopy (EIS) experiments [3]. Cox et al. anticipated that porosity provides connected paths between external oxidizing medium and the underlying metal [9]. Ni et al. reported interconnected nanopores along with grain boundaries in the oxide and concluded that development of interlinked porosity down to the metal/oxide interface is a key mechanism for the transition in oxidation kinetics [1]. Gong et al. also reported nanopores in strings formed on Zr-Nb-Y alloy and N18 alloy at grain boundaries and they suggested that initiation mechanism of porosity is Kirkendall effect [10]. In the oxide, columnar grains are more dominant in inner part and equiaxed grains are frequently observed at oxide surface. It also appears that larger columnar grains have better corrosion resistance than smaller equiaxed grains [11,12,13]. Gabory et al. showed large amorphous ZrFeNb precipitates which were observed far away (700nm) from the metal/oxide interface, while closest small amorphous β-Nb precipitates were found at 400nm position from the metal/oxide interface in ZIRLO® samples and deduced that large ZrFeNb precipitates can stay unoxidized longer in the oxide than the smaller β-Nb precipitates [14]. Despite those studies, there is still no clear understanding of oxide growth mechanism. In addition, lately, there is an attempt to increase dissolved hydrogen concentration to reduce crack growth rates of pressure boundary materials. Kass showed hydrogen pick up rate in Zircaloy-2, Ni-free Zircaloy-2 and Zircaloy-4 as a function of hydrogen pressure [15]. However, the effect of high concentration of hydrogen to zirconium fuel cladding has not been reported well.

We report here microscopic examination of early pre-transition oxide formed on ZIRLO® cladding tube samples by using scanning electron microscopy (SEM), transmission electron microscopy (TEM) with focused ion beam technique (FIB), and x-ray diffraction (XRD).

2. Materials and techniques

Commercial zirconium alloy, ZIRLO® tube has been oxidized in an autoclave of a recirculation loop at 360℃ and 20MPa for 300 hour under simulating primary water chemistry conditions (pure H2O with dissolved hydrogen of 30cc/kg, 2ppm Li as LiOH and 1200ppm B as H2BO3). The pressure difference between interior and exterior of the cladding sample was maintained at 11.7MPa during the exposure in the test loop in order to simulate the compressive stress condition in the actual fuel cladding. The sample information in this work is given in Table 1. After a corrosion test, a protective coating of platinum was deposited on the oxide surface, and then in-situ lift-out FIB sectioning was carried out on a FEI Quanta 3D FEG, instrument operated at 2-30 kV, with currents between 1pA and 65nA to prepare TEM thin foils. Fig. 1 shows an FIB-SEM image.

Table. 1. ZIRLO® tube samples investigated in this work.

	Nb	Sn	O	Fe	C	N	Hf	Zr
Composition (wt. %)	0.96	0.76	0.62	0.18	0.1	0.03	0.002	Bal.
Dimension (mm)	Outer diameter	9.5						
	Inner diameter	8.3						
	Thickness	0.6						

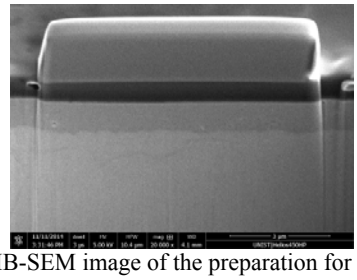

Fig. 1. An FIB-SEM image of the preparation for sectioning. A protective coating of platinum is deposited on the surface.

TEM observations were carried out on a Titan G2 at operated 300kV. The oxygen content at the metal/oxide interface and composition of second-phase particles (SPPs) were characterized respectively by energy dispersive x-ray spectroscopy (EDS) line profile and mapping. In the samples, local regions of ZrO sub-oxide can be seen in Fig. 2. The samples showed a

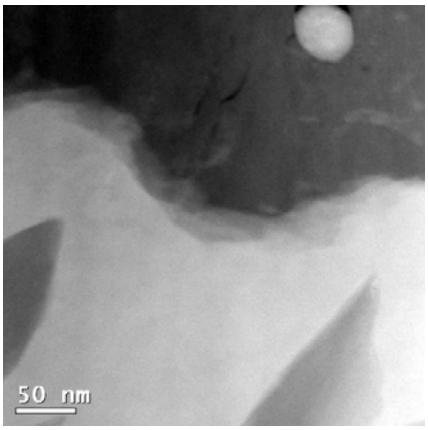

Fig. 2. Dark-field TEM image local sub-oxide along with the metal/oxide interface.

single oxide layer, it would be expected to be an early pre-transition oxide. XRD measurements were also obtained from bulk ZIRLO® tube samples of 7 mm length using a Bruker D8 ADVANCE instrument to characterize crystal structures.

3. Experimental Results

3.1 Oxide morphology

ZIRLO® tube samples corroded in 360℃ autoclave of loop for 300hour have an oxide thickness ranging from 0.9 to 1.25μm, and lateral cracks related to undulating metal/oxide interface can be clearly seen in Fig. 3. The entire oxide layer can be seen as well as

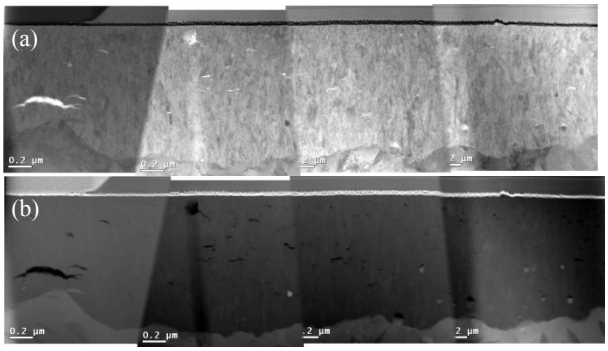

Fig. 3. (a) Bright-field TEM images showing total oxide. (b) Dark-field images of (a) .

columnar oxide grains near the metal/oxide interface. Equiaxed grains in the oxide near water/oxide interface and lateral cracks can also be observed. It seems that the cracks tend to have round shape in the outer oxide. On left side of the panorama image, a very large lateral crack is located just above the metal/oxide interface summit. It has approximately 500nm length. There is possibility that the width of this crack was extended during the FIB sectioning. Precipitates are clearly seen near the metal/oxide interface, but as getting closer to the water/oxide interface, they are gradually amorphized.

3.2 Metal/oxide interface

Dark-field TEM images show some local faint parts along the metal/oxide interface. EDS line profile of one of the faint part is given in Fig. 4. Since the faint part has Zr:O ratio of 1:1 (between 45 and 55 at.%), this part is assumed as ZrO sub-oxide layer which has about

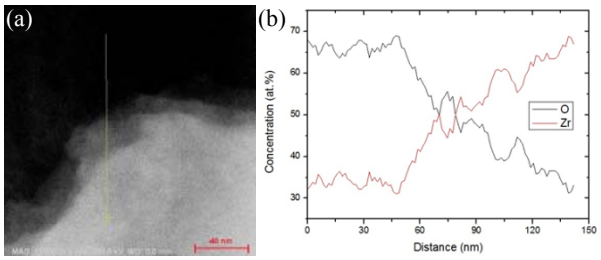

Fig. 4. (a) Dark-field TEM image of the faint part at the metal/oxide interface. (b) EDS line profile data of (a).

20nm width. EDS line profile at the interface that has no sub-oxide layer is shown in Fig. 5. On the contrary, the metal/oxide interface has a sudden change of Zr:O ratio.

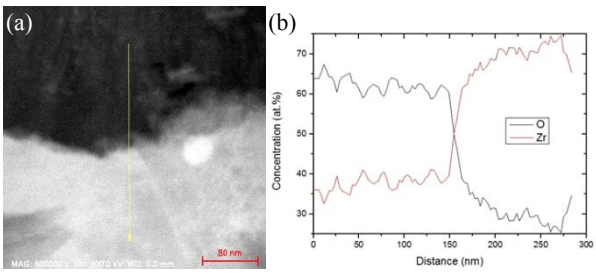

Fig. 5. (a) Dark-field TEM image of the obvious metal/oxide interface. (b) EDS line profile data of (a).

Dominance of columnar grains near the metal/oxide interface without porosity as shown in Fig. 6 demonstrates corrosion resistance of inner oxide formed on pre-transition samples.

Fig. 6 Bright-field TEM image showing columnar grains near the metal/oxide interface.

3.3 Water/oxide interface

Fig. 7 shows TEM bright/dark-field images of the oxide near water/oxide interface. In dark-field images, white dots and black spots are observed. Some black

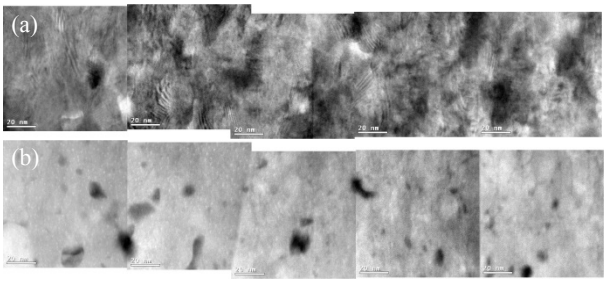

Fig. 7. (a) Bright-field TEM images of the oxide near water/oxide interface. (b) Dark-field images of (a). Some black spots of dark-field images turned into white spots in (a).

spots of dark-field images turn into white appearances on bright-field images and others do not. Therefore, it is thought that some are voids and others are amorphized precipitates. Successive images from the oxide near water/oxide interface to the metal/oxide interface are shown in Fig. 8. As images getting closer to the metal/oxide interface, the number density of black spots, which are assumed voids, tend to decrease. Finally, in the image near the metal/oxide interface, the black spots are not observed. However, white dots in the oxide near water/oxide interface could be TEM beam damage. Some of the black spots, which are assumed voids, might be contamination during FIB sample preparation.

3.4 Second-phase particles

Two types of SPPs are observed in ZIRLO® tube samples. Those are β-Nb precipitate and ZrFeNb precipitate. ZrFeNb precipitate is bigger than β-Nb precipitate, Fig. 9 shows smaller β-Nb precipitates near the metal/oxide interface. These precipitates have a crack on top, which might be an artifact during FIB sectioning. Fig. 10 shows a large ZrFeNb precipitate located at the metal/oxide interface. It also has a crack on top. The distance between outermost non-amorphized precipitate and the metal/oxide interface is 400 nm for 300 hour corroded samples.

3.5 Hydrides

Fig. 11 shows XRD peak data taken from bulk ZIRLO® tube sample. XRD data shows a weak peak of tetragonal ZrO_2 near 30° in 2-Theta comprising the great majority of α-Zr and monoclinic ZrO_2 peaks. However, zirconium hydride peak is not detected. We assume that 300 hour corrosion time in 360℃ is not enough to generate zirconium hydride or zirconium hydride may be formed too small to be detected by in-house XRD analysis.

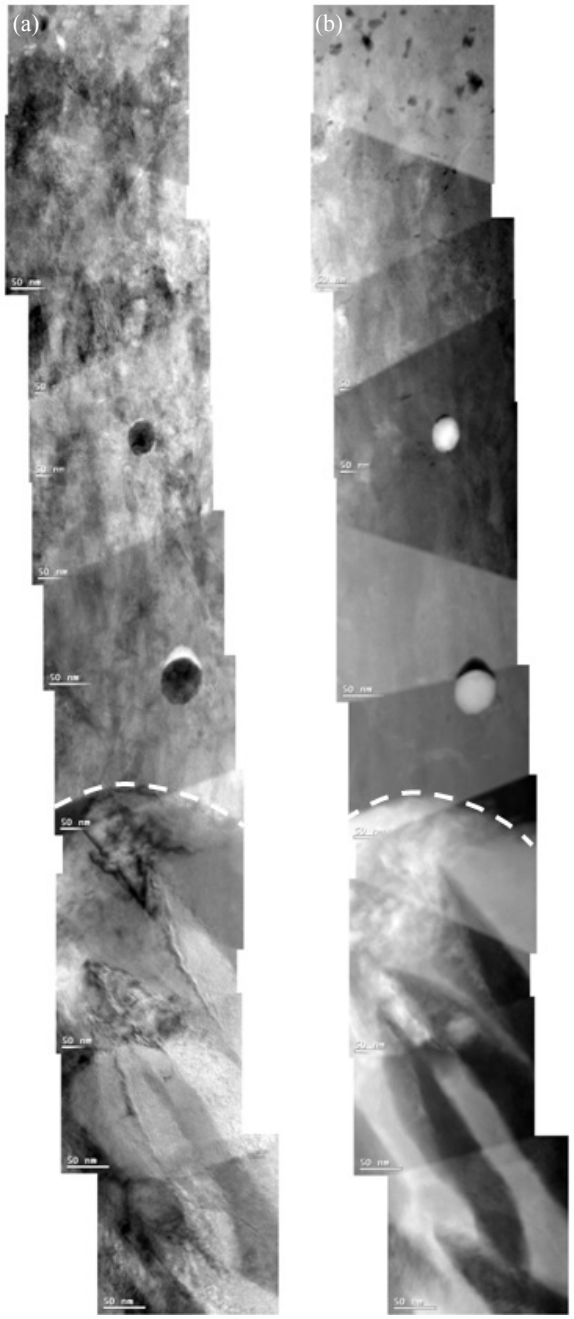

Fig. 8. (a) Bright-field TEM images from the oxide near water/oxide interface to the metal/oxide interface. (b) Dark-field images of (a). White dot lines indicate metal/oxide interface. As getting closer to the metal/oxide interface, decreasing black spots are observed.

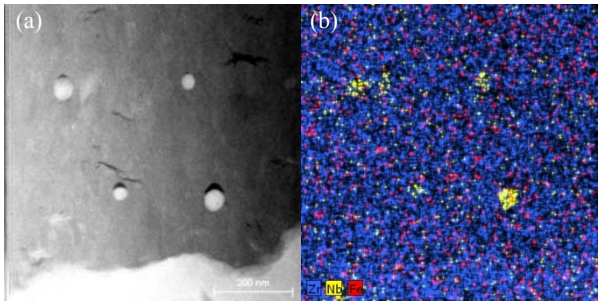

Fig. 9. (a) Smaller β-Nb precipitates with a crack on top in the oxide near metal/oxide interface. (b) EDS mapping of (a).

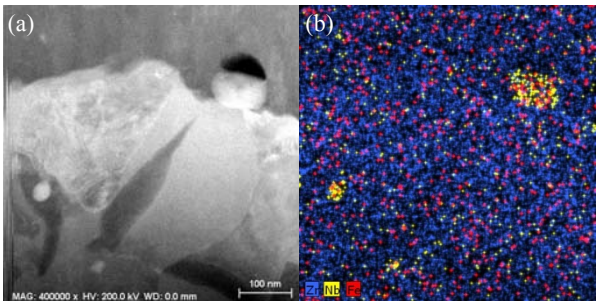

Fig. 10. (a) Bigger ZrFeNb precipitates at the metal/oxide interface. β-Nb precipitates are also observed in Zr matrix. (b) EDS mapping of (a).

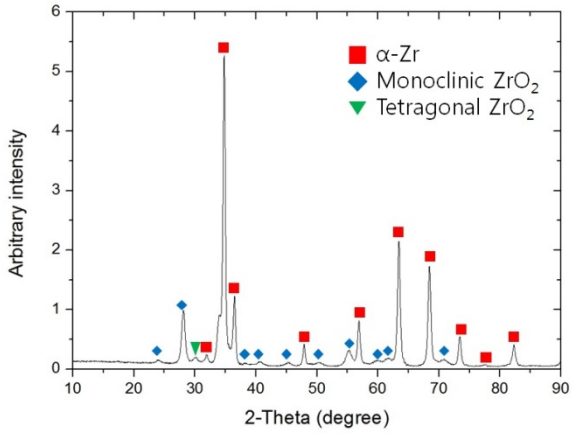

Fig. 11 XRD peak data taken from the oxidized bulk ZIRLO® tube sample.

4. Discussion

By examining oxide formed on ZILRO® tube samples which are corroded in 360℃ autoclave of loop with PWR primary water for 300hour, we report oxide morphology at the very early pre-transition stage. Such examinations for the very early pre-transition stage have not been reported well. A thin oxide layer has the thickness of 0.9~1.25μm, which shows good agreement with previous studies [16]. Local sub-oxide parts along the metal/oxide interface have approximately 20nm thickness. Ni et al. showed ~40nm thick stoichiometry ZrO layer containing unidentified grains at the metal/oxide interface of 100-day corroded ZIRLO® RXA sample [1].

Some researchers proposed that interlinked porosity at grain boundaries is a key mechanism for the transition in oxidation kinetics [1,10]. In our samples, some voids were observed and the number density of them decreased from the oxide near water/oxide interface to the metal/oxide interface. However, they might be contamination during sample preparation, beam damage, artifacts during the FIB sectioning. If the voids are contamination or beam damage during analysis process, they would be vanished through in-situ TEM heating experiments [17].

Meanwhile, other researchers suggested correlation between transition time and compressive hoop stress in the oxide layer and carried out modelling based on stress [18,19]. Lateral cracks are often observed in the oxide and on top of precipitates, especially a very large lateral crack is found just above the metal/oxide interface summit. However, these cracks might be susceptible to be widened during the FIB sectioning. In the oxide near water/oxide interface, there are cracks having round shapes. Undulation of the metal/oxide interface causing unstable stress state is believed to generate lateral cracks near the metal/oxide interface summit, whereas the cause of formation of round-shaped cracks (or cavities) near the outer oxide is not well known. We can observe two types of precipitates as far away as 400nm from the metal/oxide interface (non-amorphized precipitates), though the exact mechanism of amorphization is also not well known.

It is planned to conduct in-situ TEM heating experiments to confirm whether or not the black spots are actual voids. It is also planned to observe an initial sample (i.e., before the water exposure) and 100-day corroded post-transition cladding samples. The post-transition samples will be compared with the pre-transition samples and initial samples.

5. Conclusions

Microscopic examinations by SEM, TEM with FIB technique and XRD analysis were conducted to characterize the oxide formed on ZIRLO® cladding tube samples oxidized in an autoclave of a recirculation loop at 360℃ and 20MPa for 300 hour under simulating primary water chemistry conditions. The main conclusions are as follows:

- The samples have an oxide thickness ranging from 0.9 to 1.25μm range. Lateral cracks and columnar grains are dominant near the metal/oxide interface while round-shaped cracks (or cavities) and equiaxed grains are dominant near the water/oxide interface. A very large lateral crack is observed just above the metal/oxide interface summit that is least advanced. However, there is the possibility that the width of this crack was extended during the FIB sectioning.

- Local sub-oxide layer is shown as faint part on dark-field TEM image along the metal/oxide interface and it has Zr:O ratio of 1:1 (between 45 and 55 at.%) with about 20nm width.

- Some voids are observed in the oxide near water/oxide interface. As getting closer to the metal/oxide interface, the number density of voids tend to decrease. However, the voids might be contamination during FIB sample preparation. It is planned to conduct in-situ TEM heating experiments to confirm whether or not the voids are contamination.

- β-Nb precipitate and ZrFeNb precipitate are mainly observed. ZrFeNb precipitate is bigger than β-Nb

precipitate and both have a crack on top. This crack might be an artifact during FIB sectioning. The distance between outermost non-amorphized precipitate and the metal/oxide interface is 400 nm.

- XRD peak data taken from bulk ZIRLO® tube sample shows the great majority of α-Zr and monoclinic ZrO_2 peaks. A weak peak of tetragonal ZrO_2 is observed near 30° in 2-Theta. However, zirconium hydride peak is not detected. We assume that 300 hour corrosion time in 360℃ is not enough to generate zirconium hydride or zirconium hydride may be formed too small to be detected.

Acknowledgements

This work was financially supported by the International Collaborative Energy Technology R&D Program (No. 20138530030010) of the Korea Institute of Energy Technology Evaluation and Planning (KETEP).

REFERENCES

[1] Ni, N., Hudson, D., Wei, J., Wang, P., Lozano-Perez, S., Smith, G. D. W., ... & Grovenor, C. R. M. (2012). How the crystallography and nanoscale chemistry of the metal/oxide interface develops during the aqueous oxidation of zirconium cladding alloys. Acta Materialia, 60(20), 7132-7149.

[2] A.T. Motta, M.J.G. Da Silva, A. Yilmazbayhan, R.J. Comstock, Z. Cai, B. Lai, in: 15th International Symposium on Zr in the Nuclear Industry, Sunriver, OR, United States, American Society for Testing and Materials ASTM STP 1505, 2009, pp. 486–506.

[3] Bossis, P., Lelievre, G., Barberis, P., Iltis, X., & Lefebvre, F. (2000). Multi-scale characterization of the metal-oxide interface of zirconium alloys. ASTM SPECIAL TECHNICAL PUBLICATION, 1354, 918-942.

[4] Bryner, J. S. (1979). The cyclic nature of corrosion of Zircaloy-4 in 633 K water. Journal of nuclear materials, 82(1), 84-101.

[5] Griggs, B., Maffei, H. P., & Shannon, D. W. (1962). Multiple rate transitions in the aqueous corrosion of zircaloy. Journal of the Electrochemical Society, 109(8), 665-668.

[6] Lustman, B., & Kerze, F. (Eds.). (1955). The metallurgy of zirconium (Vol. 4). McGraw-Hill Book Company.

[7] Preuss, M., Frankel, P., Polatidis, E., Wei, J., Smith, J., Wang, C. E. F., ... & Fitzpatrick, M. (2011, August). Towards a mechanistic understanding of corrosion mechanisms in zirconium alloys. In ASTM STP1529: Zirconium in the Nuclear Industry-16th International Symposium. ASTM International.

[8] Ni, N., Lozano-Perez, S., Sykes, J. M., Smith, G. D. W., & Grovenor, C. R. M. (2011). Focussed ion beam sectioning for the 3D characterisation of cracking in oxide scales formed on commercial ZIRLO™ alloys during corrosion in high temperature pressurised water. Corrosion Science, 53(12), 4073-4083.

[9] Cox, B. (2005). Some thoughts on the mechanisms of in-reactor corrosion of zirconium alloys. Journal of Nuclear materials, 336(2), 331-368.

[10] Gong, W., Zhang, H., Wu, C., Tian, H., & Wang, X. (2013). The role of alloying elements in the initiation of nanoscale porosity in oxide films formed on zirconium alloys. Corrosion Science, 77, 391-396.

[11] Beie, H. J., Garzarolli, F., Ruhmann, H., Sell, H. J., & Mitwalsky, A. (1994). Examinations of the corrosion mechanism of zirconium alloys (No. CONF-930611--). ASTM, Philadelphia, PA (United States).

[12] Park, J. Y., Yoo, S. J., Choi, B. K., & Jeong, Y. H. (2007). Oxide microstructures of advanced Zr alloys corroded in 360 C water loop. Journal of alloys and compounds, 437(1), 274-279.

[13] Yilmazbayhan, A., Breval, E., Motta, A. T., & Comstock, R. J. (2006). Transmission electron microscopy examination of oxide layers formed on Zr alloys. Journal of Nuclear Materials, 349(3), 265-281.

[14] de Gabory, B., Motta, A. T., & Wang, K. (2015). Transmission electron microscopy characterization of Zircaloy-4 and ZIRLO™ oxide layers. Journal of Nuclear Materials, 456, 272-280.

[15] Kass, S. (1963). ASTM, STP 368. In Symposium Corrosium of Zirconium alloys.

[16] Wei, J., Frankel, P., Polatidis, E., Blat, M., Ambard, A., Comstock, R. J., ... & Preuss, M. (2013). The effect of Sn on autoclave corrosion performance and corrosion mechanisms in Zr–Sn–Nb alloys. Acta Materialia, 61(11), 4200-4214.

[17] Kim, H. G., Kim, I. H., Park, J. Y., Yoo, S. J., & Kim, J. G. (2014). In situ heating TEM analysis of oxide layer formed on Zr–1.5 Nb alloy. Journal of Nuclear Materials, 451(1), 189-197.

[18] Ly, A., Ambard, A., Blat-Yrieix, M., Legras, L., Frankel, P., Preuss, M., ... & Bréchet, Y. (2011). Understanding crack formation at the metal/oxide interface during corrosion of Zircaloy-4 using a simple mechanical Model. In in press in the Journal of ASTM International (Proceedings of the 16th International Symposium on the Zirconium in the Nuclear Industry, 2010, Chengdu, Sichuan Province, Chin (9th May 2010–13th May).

[19] Parise, M., Sicardy, O., & Cailletaud, G. (1998). Modelling of the mechanical behavior of the metal–oxide system during Zr alloy oxidation. Journal of nuclear materials, 256(1), 35-46.